



2D and 3D orientation mapping in nanostructured metals

A review

Wu, Guilin; Zhu, Wanquan; He, Qiongyao; Feng, Zongqiang; Huang, Tianlin; Zhang, Ling; Schmidt, Søren; Godfrey, Andrew; Huang, Xiaoxu

Published in:
Nano Materials Science

Link to article, DOI:
[10.1016/j.nanoms.2020.03.006](https://doi.org/10.1016/j.nanoms.2020.03.006)

Publication date:
2020

Document Version
Publisher's PDF, also known as Version of record

[Link back to DTU Orbit](#)

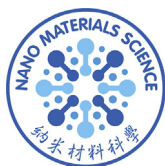
Citation (APA):
Wu, G., Zhu, W., He, Q., Feng, Z., Huang, T., Zhang, L., Schmidt, S., Godfrey, A., & Huang, X. (2020). 2D and 3D orientation mapping in nanostructured metals: A review. *Nano Materials Science*, 2(1), 50-57.
<https://doi.org/10.1016/j.nanoms.2020.03.006>

General rights

Copyright and moral rights for the publications made accessible in the public portal are retained by the authors and/or other copyright owners and it is a condition of accessing publications that users recognise and abide by the legal requirements associated with these rights.

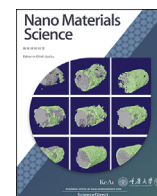
- Users may download and print one copy of any publication from the public portal for the purpose of private study or research.
- You may not further distribute the material or use it for any profit-making activity or commercial gain
- You may freely distribute the URL identifying the publication in the public portal

If you believe that this document breaches copyright please contact us providing details, and we will remove access to the work immediately and investigate your claim.



Contents lists available at ScienceDirect

Nano Materials Science

journal homepage: www.keaipublishing.com/cn/journals/nano-materials-science/

2D and 3D orientation mapping in nanostructured metals: A review

Guilin Wu^{a,b,*}, Wanquan Zhu^{a,b}, Qiongyao He^a, Zongqiang Feng^{a,b}, Tianlin Huang^{a,c},
Ling Zhang^{a,b}, Søren Schmidt^d, Andrew Godfrey^e, Xiaoxu Huang^{a,b}

^a International Joint Laboratory for Light Alloys (MOE), College of Materials Science and Engineering, Chongqing University, Chongqing, 400044, China

^b Shenyang National Laboratory for Materials Sciences, Chongqing University, Chongqing, 400044, China

^c Electron Microscopy Center of Chongqing University, Chongqing University, Chongqing, 400044, China

^d Department of Physics, Technical University of Denmark, DK-2800 Kgs. Lyngby, Denmark

^e Laboratory of Advanced Materials (MOE), School of Materials Science and Engineering, Tsinghua University, Beijing, 100184, China

ARTICLE INFO

Keywords:

Nanostructured metals
Microstructure
Crystallographic orientation
EBSD
PED
3D-OMiTEM

ABSTRACT

Nanostructured metals possess various excellent properties and offer the potential for a wide range of applications. Improvements in the properties and performance of nanostructured metal components motivate a complete characterization of the microstructures and crystallographic orientations of nanostructured metals with nanoscale spatial resolution. Two well developed orientation mapping techniques for such characterization are electron backscatter diffraction (EBSD) in the scanning electron microscope and precession electron diffraction (PED) using diffraction spots in the transmission electron microscope. However, these methods can only characterize the structure in two dimensions. It is still a great challenge to characterize grains in three dimensions, i.e. from the interior of the nanostructured metals. Recently, three-dimensional orientation mapping in the transmission electron microscope (3D-OMiTEM) was developed and further improvements of this technique are introduced in this paper. Utilization of these orientation mapping techniques for structural and orientational characterizations are demonstrated by examples of surface-deformed metals with gradient nanostructures, and a sputtered gold film of nano-islands containing nanograins. The merits and challenges of each of these techniques are discussed and suggestions for further developments are proposed.

1. Introduction

Nanostructured metals have attracted much research interest over the past two decades on account of their excellent mechanical, physical, chemical and other properties [1–6]. Already a number of applications of nanostructured metals can be found in the fields such as microelectronics, nanotechnology and catalysis. The properties and performance of the components in micro-electronics structures and ensembles of catalysts are, to a large extent, determined by the morphologies, sizes/volumes, crystallographic orientations, etc., of the individual nano-sized grains in such nanostructured metals. To understand and further improve nanostructured metals, a detailed and complete characterization of these structural parameters, especially the crystallographic orientations, at high nanoscale spatial resolution, is therefore required. Electron microscopes are well adapted to fulfill such requirement because of their high spatial resolution. In the past decades, various electron microscope techniques have been developed for orientation determination. In these

techniques the orientations are typically determined either using Kikuchi patterns, both in the scanning electron microscope (SEM) [7,8] and in the transmission electron microscope (TEM) [9,10], or using diffraction spot patterns (including directly obtained patterns and reconstructed diffraction patterns, i.e. by dark field conical scanning) in the TEM [10–13]. Based on such spatially resolved data, individual orientations can be displayed on a regular grid so that the characterized microstructures can be reconstructed. This method of microstructure reconstruction based on crystallographic orientations is normally called orientation mapping.

The most popular orientation mapping techniques include (but are not limited to) electron backscatter diffraction (EBSD) in the SEM [7,8], automated two-dimensional (2D) precession electron diffraction (PED) in the TEM [14,15] and three-dimensional orientation mapping in the transmission electron microscope (3D-OMiTEM) [16]. The angular resolutions of these techniques are 1–2° or better depending on the microscope working conditions and the state of materials under investigation.

* Corresponding author. International Joint Laboratory for Light Alloys (MOE), College of Materials Science and Engineering, Chongqing University, Chongqing, 400044, China.

E-mail address: wugl@cqu.edu.cn (G. Wu).

<https://doi.org/10.1016/j.nanoms.2020.03.006>

Received 9 March 2020; Accepted 22 March 2020

Available online 24 March 2020

2589-9651/© 2020 Chongqing University. Production and hosting by Elsevier B.V. on behalf of KeAi. This is an open access article under the CC BY-NC-ND license

(<http://creativecommons.org/licenses/by-nc-nd/4.0/>).

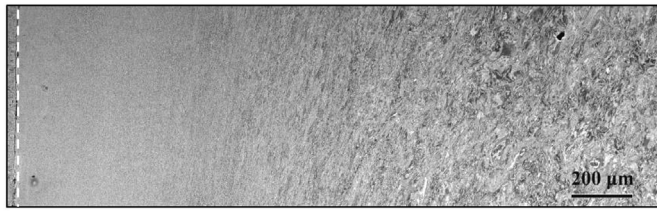


Fig. 1. A low magnification ECC image showing a gradient structure observed from the tangential section of a sample of pure Cu processed by high pressure surface rolling [26]. The dashed white line marks the surface.

Such angular resolutions are suitable for mapping nanostructured metals produced by different processes as they are mainly characterized by boundaries of misorientation angles larger than 1° . However, the differences in the spatial resolution are significant among these techniques, and this determines the selection of appropriate techniques for mapping nanostructured metals of different characteristic scales.

In this paper, we provide a brief review on the use of the 2D and 3D orientation mapping techniques for structural and orientational characterizations in nanostructured metals with a particular focus on the spatial resolution of these techniques. The use of SEM-based 2D EBSD and TEM-based 2D PED techniques is demonstrated by examples of characterizing surface deformation induced gradient nanostructures, where the structural scales vary over a wide range from about a few nanometers to several hundred nanometers. The use of 3D-OMiTEM is demonstrated by characterization of a gold nano-island film, where the structure is relatively uniform and on a length scale of less than 100 nm. The microstructural parameters and crystallographic characteristics of these

nanostructured metals are analyzed and some merits and challenges regarding each technique are discussed, with further developments suggested.

2. 2D Grain orientation mapping of gradient nanostructured metals

Several different techniques involving surface plastic deformation have been developed for generating gradient nanostructures at a metal surface, including surface mechanical attrition treatment [17–19], modified shot-peening [20,21], surface mechanical grinding treatment (SMGT) [22], frictional sliding deformation [23–25] and high-pressure surface rolling (HPSR) [26]. Two of the important characteristics associated with the resulting surface gradient nanostructures are the microstructural gradient and the textural gradient [1,24], and each of these results directly from the strain gradient and strain-rate gradient generated by the applied surface plastic deformation. The details of the structural and textural gradients depend therefore on the processing technique and the processing conditions, as well as on material parameters. Such precise characterization of the microstructural and textural gradients is very important for guide the improvement of properties and performance of metallic components treated to produce such gradients.

The range of grain sizes of a gradient nanostructured metal is arguably the most important parameter to consider when choosing a relevant grain orientation mapping technique. In this section, two examples of grain orientation mapping, by 2D SEM-based EBSD and by TEM-based PED techniques, are given to show how microstructural and textural information can be obtained in surface gradient nanostructured metals.

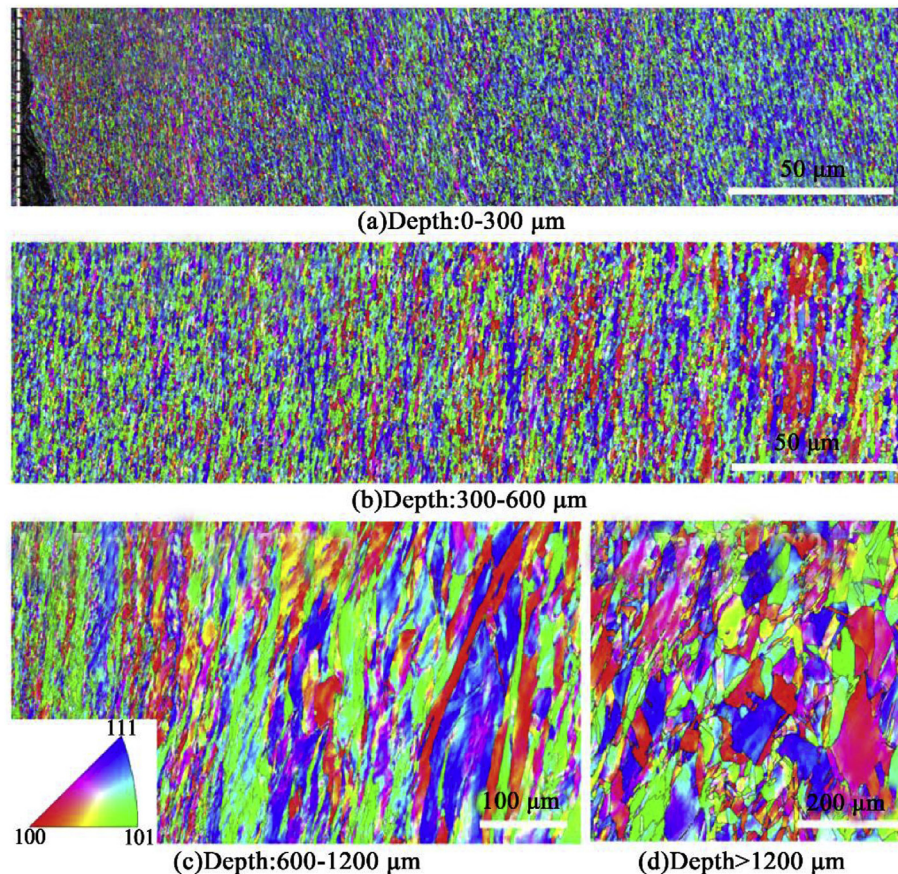


Fig. 2. EBSD maps at various depths from the surface in HPSR-processed Cu [26] (same sample as shown in Fig. 1). (a) 0–300 μm , (b) 300–600 μm , (c) 600–1200 μm , and (d) > 1200 μm . The white dashed line in (a) indicates the surface. Non-indexed points, which are related mainly to grain boundaries and second phase particles, are shown in black.

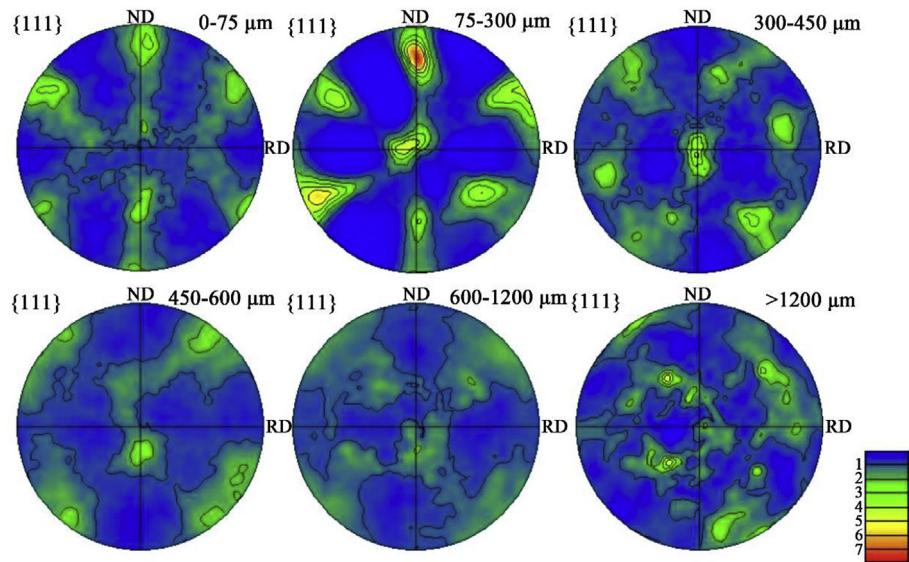


Fig. 3. $\{111\}$ pole figures generated from the EBSD data shown in Fig. 2 [27]. Note that some of the original EBSD data sets were divided into subsets along the depth for plotting the pole figures.

2.1. Grain orientation mapping by SEM-based EBSD

Fig. 1 shows a SEM electron channeling contrast (ECC) image of a pure Cu sample processed by HPSR [26] covering the entire deformed layer, from the surface (dashed line) to the coarse grains in the undeformed matrix 2 mm below the surface. The sample illustrates typical features of a gradient microstructure.

Grain orientation mapping was carried out for a series of maps taken along the depth direction in the HPSR-processed Cu, as shown in Fig. 2 [26]. In these maps, black dots indicate unindexed points. A gradient

structure from the topmost surface to the coarse-grained bulk is clearly observed in Fig. 2(a–d). The black layer on the left side of Fig. 2 (a) corresponds to the microstructure in the top $\sim 10 \mu\text{m}$ in Fig. 1. In this layer details of the microstructure cannot be resolved using EBSD on account of both the fine grains and the high density of defects within the grains. At depths of 10–600 μm , an indexing fraction rate of about 73–75% is achieved. The orientation maps (Fig. 2(a) and (b)) reveal a lamellar structure parallel to the sample surface with a gradual increase of the boundary spacing from 110 nm at a depth of $\sim 20 \mu\text{m}$ to about 580 nm at a depth of 600 μm . The indexing fraction further increases to

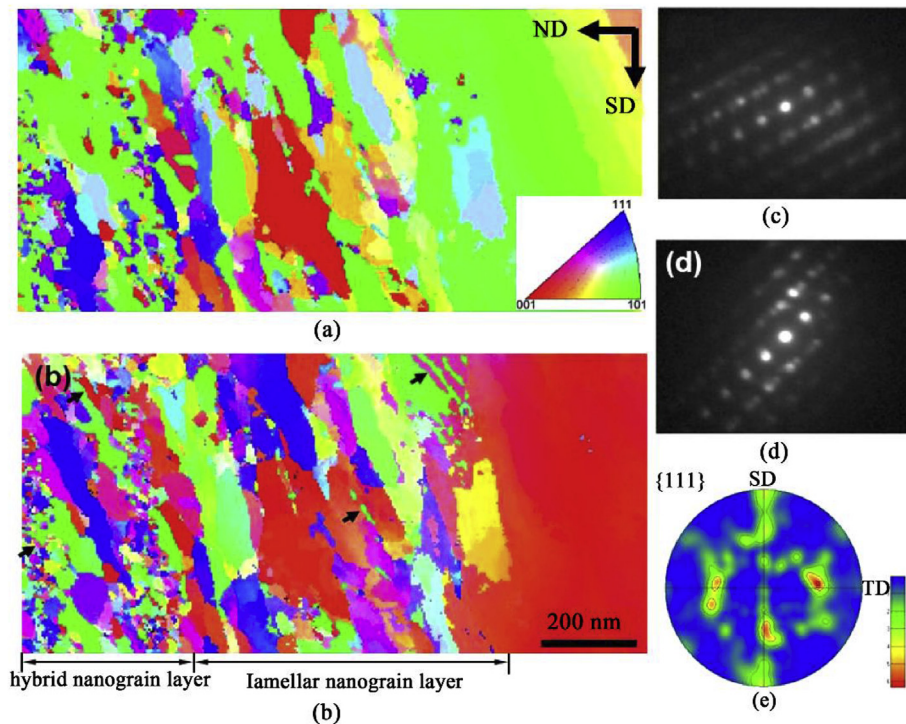


Fig. 4. TEM-based PED orientation maps obtained in the topmost surface layer of a Ni-based alloy plate sample processed by a surface mechanical grinding treatment [33]. (a, b) SD and ND inverse pole figure maps. (c, d) PED patterns obtained from locations A and B as shown in (a) containing fine deformation twins. (e) $\{111\}$ pole figure obtained from the entire mapped region.

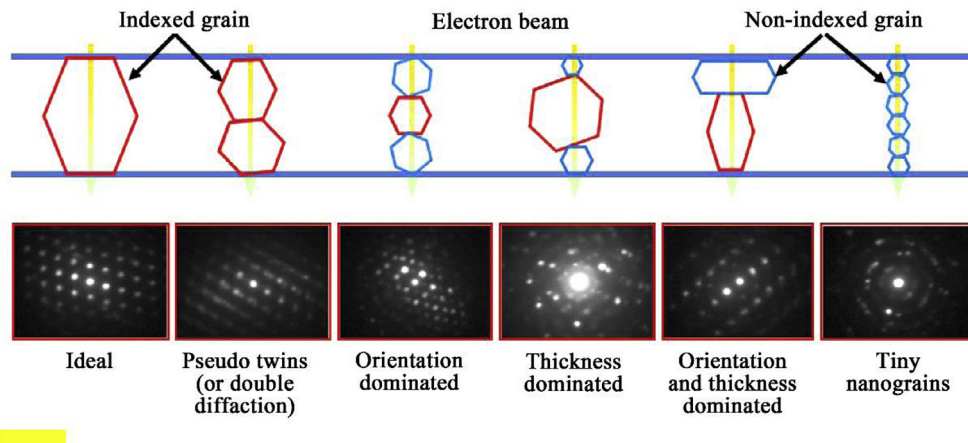


Fig. 5. Examples of possible situations of grain overlapping that may cause difficulties in indexing grain orientation and generating reliable grain orientation maps. In the map, red grains represent the grains that can be indexed; while blue grains represent the grains that cannot be indexed.

84% in the depth range of 600–1200 μm , where a transition region is formed, composed of the lamellar structure and slightly refined grains (Fig. 2 (c)). At depths greater than 1200 μm , the indexing fraction is about 95% (Fig. 2 (d)). As seen in the right side of Fig. 2 (d) the grains are slightly deformed but otherwise are similar in appearance to those in the unaffected annealed microstructure at depths larger than 2000 μm .

Fig. 3 shows $\{111\}$ pole figures corresponding to the material at different depths, and illustrates the evolution of texture in the HPSR treated Cu sample with increasing deformation [27]. Here ND refers to the normal direction of the surface-deformed plate and RD refers to the rolling direction (the tangential direction of the rotating rollers used in the surface-deformation process), which is parallel to the vertical direction of the EBSD map in Fig. 2. It is seen that in the surface region (0–75 μm) a weak shear texture with dominant $\{001\}\langle 110 \rangle$ and $\{111\}\langle 110 \rangle$ components is formed. One interesting observation is that the shear texture is stronger in the volume 75–300 μm from the surface. At larger depths (300–450 μm) the texture is dominated by the components close to the Brass and Copper components. At still further depth from the surface the texture becomes weaker. The development of well-defined shear texture components in the surface region suggests that the HPSR processing results in strong shear deformation at the surface, similar to that reported during sliding [23] and SMT [22].

As shown in Fig. 2, the topmost layer of the HPSR-processed Cu cannot be indexed by the SEM-based EBSD technique, even though these maps were obtained using a field-emission gun SEM. However, the boundary spacing (grain size) can be estimated from high-magnification ECC observations [26], where a finest boundary spacing of about 50 nm is observed in this layer. SEM-based EBSD is nowadays the most popular technique for orientation mapping. The spatial resolution depends on the mean atomic number, Z , of the examined material, and on other operating parameters, such as the accelerating voltage, beam current, as well as the internal strain and defect density of the examined material. Higher spatial resolution than in the present experiment has been reported [28] for example for fully recrystallized grains. However, it is generally agreed that the practical spatial resolution under normal conditions is on the order of 20–50 nm. The biggest limitation in the spatial resolution of EBSD is related to the excitation volume resulting from electron beam interactions in the examined material. Various methods have been proposed to improve the spatial resolution of EBSD, such as reduction of the accelerating voltage [29]. Another successful method where a higher spatial resolution has been achieved is transmission EBSD (t-EBSD) [30, 31]. The essential point of this method is a reduction in the interaction volume, achieved by changing the EBSD geometry to allow the use of thin foil TEM samples. Such methods are still limited however by the beam-sizes that can be formed in a SEM instrument. As outlined in the next section a further improvement in orientation mapping can be

achieved by using a TEM.

2.2. Grain orientation mapping by TEM-based PED

The TEM has much higher spatial resolution than the SEM, mainly due to its much smaller electron beam spot size. As such, a series of orientation mapping techniques in the TEM have been developed, including automated crystal orientation mapping based on PED.

The TEM-based PED method is a proven and a useful quantitative technique allowing grain size and texture analysis with a spatial resolution down to a few nanometers [15,32]. This technique has been used already for mapping grain orientations in the surface gradient nanostructures of several metals and alloys [33–35] generated by the applications of different surface plastic deformation treatments. Fig. 4 shows an example of orientation maps obtained in a commercial Ni-based superalloy plate processed by flat surface mechanical grinding [33]. In this figure, the plate surface normal direction is defined as ND and the grinding direction is defined as SD [33]. Also shown in this figure are inverse pole figure maps for SD and for ND covering only the topmost 1.3 μm -thick layer [33] of a deformed sample (Fig. 4(a)). A clear gradient structure is seen, composed of a 350 nm-thick layer of mixed equiaxed and lamellar nanograins, and a 650 nm-thick lamellar nanograin layer. Deformation twins (indicated by arrows) as fine as 8 nm can be also recognized by indexing the PED patterns; examples are shown in Fig. 4(c) and (d). Based on the PED orientation mapping, the crystallographic texture of the surface deformed layer was identified as a mixture of a strong shear texture component, $\{001\}\langle 110 \rangle$, and a minor Copper component, $\{112\}\langle 111 \rangle$. The formation of shear texture components is a result of the shear deformation introduced by the surface grinding process.

One of the difficult challenges for the TEM-based PED method is determination of crystallite orientations in the topmost layer of gradient nanostructures, as even in a thin-film sample there may be overlapping grains in the through-thickness direction, with the recorded diffraction signal arising from more than one grain. Fig. 5 shows examples of possible situations where grains overlapping through the sample thickness may generate difficulties in achieving correct indexing of the grain orientations. The situation on the far left shows the ideal case in which the sample thickness consists only of a single grain and therefore results in a single diffraction pattern that can be easily indexed. When two or more grains are overlapping along the electron beam direction (the remaining cases shown in Fig. 5), more complicated diffraction patterns will be arise, and in these patterns one or more sets of diffraction patterns may dominant depending on their orientation or volume dominance. The orientation-dominated situation will arise in the case of one grain has a low index zone axis close to the beam direction and thus forms a

diffraction pattern with a high intensity. In the case of a large grain with such an orientation dominance, the diffraction pattern may be dominated by one spot pattern, even though the electron beam passes through more than one grain. A more general case, resulting in a more complicated diffraction pattern, is where several grains with similar dominance of orientation and volume overlap in the through-thickness direction, and the corresponding diffraction pattern is a superposition of patterns with similar intensities from the overlapping grains. This will lead to confusion in the PED template-matching procedure. Additional the fact that the PED technique assigns one orientation to each mapped location may also result in errors in the orientation map, as no depth information regarding the origin of diffraction signal for the indexed grains is available. As such grains that appear to be adjacent on the projected 2D map may not in fact be neighboring grains in the sample volume.

The challenges in quantitative crystallographic characterization using TEM-based spot diffraction methods, including PED, have been discussed in detail by Bobler and Kübel [36]. In their study tilt series data were collected over an angular range of 10° for a nanocrystalline Pd thin film to see how the overlapping grains were revealed at different tilts. It was found that many overlapping grains appeared and disappeared depending on the tilt angle and the evaluation parameters chosen for the cross-correlation between the experimental and simulated (template) diffraction patterns. The results of this study also revealed that some orientations were more dominant than others during the template-matching procedure between experimental and simulated diffraction patterns, and that a measure of high reliability was not a sufficient criterion to exclude overlapping grains.

The challenge in indexing superimposed diffraction patterns that may arise from overlapping grains is an inherent problem in the study of nanostructured materials for any TEM-based technique, including the 2D dark field conical scanning technique [12,13], as well as for the SEM-based t-EBSD method [30,31]. In order to overcome this limitation and to distinguish the diffraction signal from overlapping nanograins, 3D orientation mapping techniques are thus required where diffraction signal from overlapping nanograins can be resolved, allowing accurate three-dimensional spatial information.

3. 3D grain orientation mapping of a gold nano-island film

Noble metal (i.e. Au, Ag) nano-island films or nanoparticle films have a diverse range of applications in fields such as catalysis, energy, biology, and nanotechnology and have recently attracted much attention [5,6]. The performance and reliability of these nanomaterials are controlled by structural parameters such as the morphology [37] and the crystallographic orientations of the films [38], as well as of any defects present (such as multiple twin structures [39]). Detailed characterization of these structural parameters is therefore essential both to allow the development of improving synthesis methods and to facilitate a better understanding the functionality of this class of nanomaterials. Traditional SEM and TEM methods have been used to characterize the crystallographic and morphological characteristics of nano-islands or nanoparticles. In such materials, however, each nano-island or particle may consist of a group of grains that may also overlap in the thickness direction of the thin film, and as such a three-dimensional technique is required for a full characterization of the morphology and crystallography of the nano-islands or nanoparticles in these films [36,40].

In a recent study [41], a gold nano-island film, deposited by ion sputtering at room temperature in a vacuum, was characterized by an improved 3D-OMiTEM. The raw data for 3D grain orientation mapping are dark field images acquired by combining dark field conical scanning [16] and sample tilting. The data acquisition was carried out using a JEM-2100 TEM equipped with a fast TVIPS camera and the EM-Tool software system, allowing image recording at a speed of more than 20 fps. This data acquisition speed is 10 times faster than the first implementation of the 3D-OMiTEM technique [16]. Detailed procedures of the dark field conical scanning procedure at each sample tilt are described in

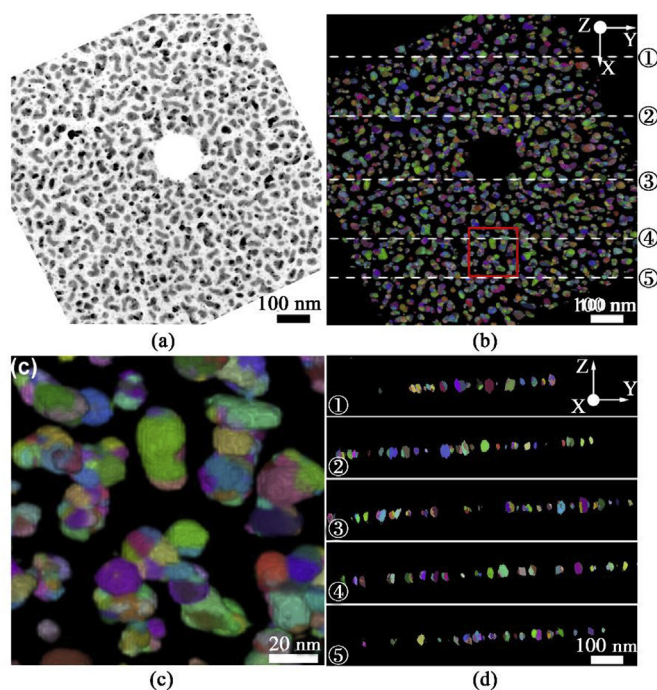


Fig. 6. A gold nano-island film and its orientation mapping [41]. (a) TEM image showing the distribution of gold nano-islands in the prepared film. (b) Plane view of a reconstructed 3D orientation map. (c) Enlarged view of the area marked by the red square-frame in (b). (d) Five cross-sectional (through thickness) views of the reconstructed 3D orientation map of the gold nano-island film. The colours in the maps represent the crystallographic orientations of the grains; the white dashed lines in (b) indicate the locations where the Y-Z cross-sectional views in (d) are obtained.

[41]. The conical scanning process was repeated at different sample tilts over the range of -70° to $+70^\circ$ at steps of 1° using an EM-2131HTR single high tilt holder. In total, more than 200,000 dark field images were recorded for the orientation analysis and 3D reconstruction.

In addition to an enhancement in data collection speed, significant improvements have been achieved in the data processing since this technique was first proposed [16]. These include tomographic alignment at different sample tilts, carried out by calculating the image drift using a subpixel image registration algorithm [42], and tilt axis correction determined from the fast Fourier transformation (FFT) of the average intensity projection of all bright field images [43]. An adaptive spatial filter [44] was also used to improve the signal-to-noise ratio of the dark field images. Additionally, reliable intensity transformation [45] and binarization functions [46,47] have been applied to the dark field images. The final 3D orientation map was reconstructed using a dictionary-based forward indexing algorithm. The final reconstructed data set comprised a volume of $200 \times 1024 \times 1024 \text{ nm}^3$ with a resolution of $1 \text{ nm}^3/\text{voxel}$. An in-house code modified from the algorithm described in Ref. [48] was applied to identify the grains in the 3D orientation map. Values of equivalent sphere radius (ESR) were calculated [49,50] for both the islands and the grains inside each island.

Fig. 6 (a) shows a bright field TEM image of a region of the film where the gold nano-islands are uniformly distributed. It can be seen some islands are equiaxed whereas others have an elongated rod shape. Fig. 6 (b) shows a plane view of the reconstructed 3D orientation map of the same area. Note that the sample coordinate system shown in Fig. 6 (b) was defined with the X direction parallel to the sample tilt axis, the Z direction parallel the electron beam, and the Y direction as a cross product of the Z and X directions. Fig. 6 (c) shows an enlarged view of the area marked by a square frame in Fig. 6 (b). Several remarkable features of these results can be noted, including: (1) there is a one-to-one correspondence between the islands seen in the bright field image (Fig. 6 (a))

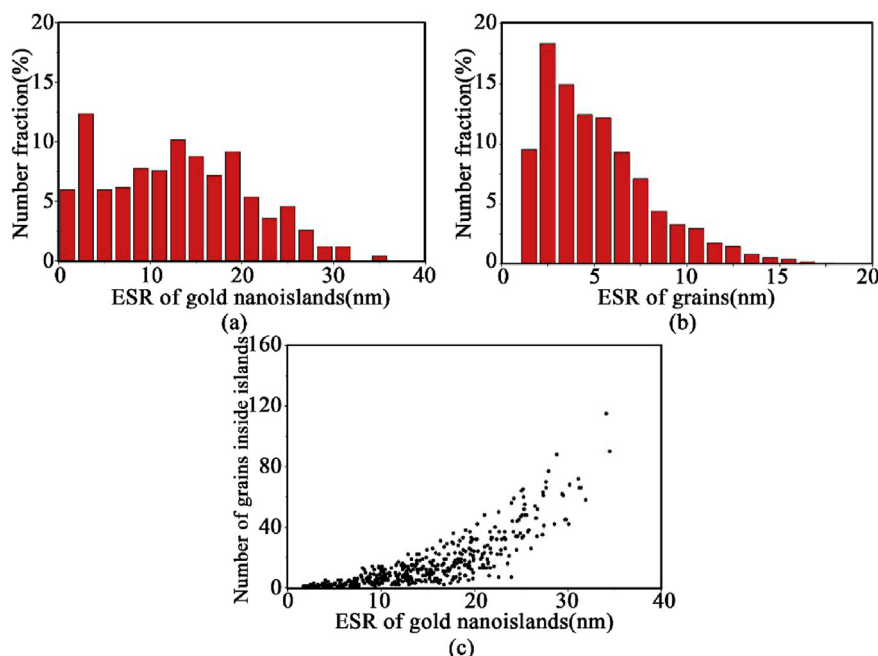


Fig. 7. Histograms showing sizes, expressed at the equivalent spherical radius (ESR), of gold nano-islands (a) and grains inside the nano-islands (b). (c) Relationship between the number of grains inside individual islands and the ESR of gold nano-islands [41].

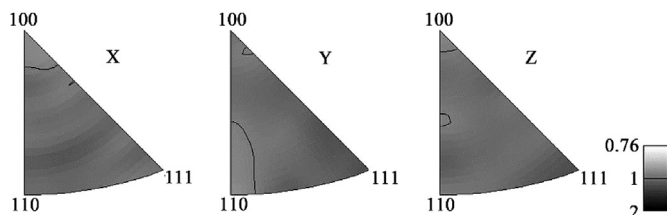


Fig. 8. Unit triangle projections showing the distribution of orientations of the grains in the gold nano-island film [41].

and in the orientation map (Fig. 6 (b)); (2) most of the islands are composed of a cluster of grains of different orientations; and (3) the grains within a given island vary significantly in size. To illustrate this further Fig. 6 (d) shows five slices of the 3D orientation map, illustrating the morphological and crystallographic features through the film thickness (Z-direction). It is seen that for some islands the grains penetrate through the film thickness while for others the grains overlap on top of each other.

In the final reconstructed 3D orientation map, more than 500 islands and 7000 grains can be identified. Histograms of the ESRs calculated for the islands and for the grains are shown in Fig. 7(a) and (b), respectively, with both showing a wide distribution. The average ESRs of islands and grains are 13 nm and 5.3 nm, respectively. The smallest diameter of a 3D reconstructed grain is only 3.4 nm (ESR = 1.7 nm), highlighting the high spatial resolution of the improved 3D-OMiTEM technique. Fig. 7 (c) shows the correlation between the number of grains inside individual islands and the ESR of the gold nano-islands. It is seen that on average the number of grains inside an island increases with increasing island ESR, although the values vary within a certain range. From a stereological analysis, the average number of grains within one island should be $(13/5.3)^3 = 14.8$, which is in a good agreement with the measured average number of 14.

Fig. 8 shows the distribution of the X, Y and Z axis directions for all the identified grains in a standard unit triangle projection. It can be seen that the gold island film has a very weak texture, indicating that the grains in the nano-island film are rather randomly oriented.

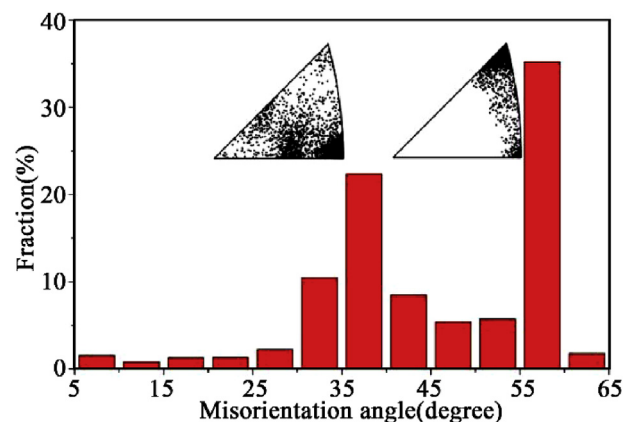


Fig. 9. Distribution of misorientation angles across the grain boundaries in gold nano-islands [41]. Insets show the rotation axes corresponding to the misorientation peaks at 40° and 60°.

Fig. 9 shows the distribution of misorientation angles for all identified grain boundaries in the mapped nano-island volume, using a cut-off angle of 5°. Two clear peaks, around misorientation angles of 40° and 60° are seen. Their corresponding rotation axes are given in the two inset unit triangles, and showing strong a strong concentration of axes near <110> and <111>, respectively. These observations indicate that the presence of large fractions of $\Sigma 9$ and $\Sigma 3$ boundaries in the islands, which is considered to be related to the formation of first order ($\Sigma 3$) and second order ($\Sigma 9$) growth twins in the gold nano-islands during the sputtering process.

3D orientation mapping based on the acquisition of diffraction patterns for every pixel, at every tilt, is possible [51,52] if individual diffraction signals from superimposed diffraction patterns can be separated [13], for example using the principal component analysis method [53]. However, such a direct diffraction tomography technique for 3D grain orientation mapping is not yet available. Instead, the present 3D orientation mapping technique has been developed based on dark field conical scanning over a large region of reciprocal space and using a series of sample tilts [16]. This technique enables a precise and complete

identification of the size, orientation, location and neighborhood relationship of grains in the sample volume.

Remaining issues with this technique include the data acquisition speed, possible distortions of the 3D grain orientation map caused by the missing wedge effect, and the robustness of 3D reconstruction algorithm. As can be seen in Fig. 6 (d) many grains are seen to be elongated in the film thickness direction. Part of the reason for this elongated morphology is related to the “missing wedge” effect [54], which arises due to the restricted available tilt angle range in this experiment of $\pm 70^\circ$ for data acquisition. However, the aspect ratio of the grains that penetrate the film thickness (Fig. 6 (d)) is obviously larger than 1.1, which is the value expected for the distortion in the film thickness direction from a “missing wedge” effect using a tilt angle range of $\pm 70^\circ$ [54]. Therefore, the elongated morphology of the grains is believed to be real and may result from grain growth taking from the sputtering conditions used for the sample preparation. To remove any “missing wedge” effects, for better detailed morphological characterization of the shapes of grains and islands, a tilt angle of 180° or larger for data acquisition is required. In this regard the use of a 360° rotation TEM sample holder [55,56] is currently being explored for the OMiTEM technique.

4. Concluding remarks

In this paper we have shown how two-dimensional SEM-based EBSD and TEM-based PED techniques can be applied to obtain grain orientation maps, providing useful information on microstructural and textural gradients. The resulting data clearly demonstrate that surface plastic deformation can serve as an approach to produce surface gradient nanostructures in metals and alloys with characteristic microstructural and textural gradients. However, limitations and challenges still remain for both types of technique. The SEM-based EBSD technique, despite significant technological development in recent years, is still limited by the EBSD signal source volume to a resolution in the order of 20–50 nm, which is insufficient to measure accurately orientations of nanograins in the topmost layer of gradient nanostructured metals. The TEM-based PED method has been proven to be able to measure the orientation of grains as small as a few nanometers. However, at this length scale it remains a challenge to correctly distinguish and solve superimposed diffraction patterns from overlapping grains aligned along the beam direction. A similar problem exists also for the TEM-based 2D dark field conical scanning technique and for the SEM-based t-EBSD method.

As a demonstration of an improved version of the 3D-OMiTEM technique we have shown that it is possible to successfully characterize the 3D morphological and crystallographic characteristics of a gold nano-island film. For this a volume of $200 \times 1024 \times 1024 \text{ nm}^3$ was reconstructed, within which a 3D orientation map of islands and grains has been generated and analyzed. The diameter of the smallest grain identified is 3.4 nm, demonstrating the high spatial resolution of the 3D-OMiTEM technique. In some islands many grains penetrate the full film thickness, while other islands are composed of many grains overlapping each other in the film through-thickness direction. Grains penetrating the film thickness show clear elongation along the film thickness direction, though such an elongation is partly attributable to the “missing-wedge effect” due to the limited tilt angle range used for data collection. Further improvement of the data acquisition using a 360° rotation sample holder in TEM is required for a more accurate evaluation of the grain geometry, and such an effort is underway.

Acknowledgements

This work was supported by the National Key Research and Development Program of China (2016YFB0700400) and National Natural Science Foundation of China (Nos. 51327805, 51971045, 51971043 and 51671039). SS thanks the support of the “111 Project” (B16007) by the Ministry of Education and the State Administration of Foreign Experts Affairs, China.

References

- [1] X.C. Liu, H.W. Zhang, K. Lu, *Science* 342 (2013) 337–340, <https://doi.org/10.1126/science.1242578>.
- [2] G. Wu, K.C. Chan, L. Zhu, L. Sun, J. Lu, *Nature* 545 (2017) 80–83, <https://doi.org/10.1038/nature21691>.
- [3] L. Lu, Y.F. Shen, X.H. Chen, L.H. Qian, K. Lu, *Science* 304 (2004) 422–426, <https://doi.org/10.1126/science.1092905>.
- [4] X. Zhou, X.Y. Li, K. Lu, *Science* 360 (2018) 526–530, <https://doi.org/10.1126/science.aar6941>.
- [5] S. Zaefferer, *Catal. Today* 72 (2002) 11–17, [https://doi.org/10.1016/S0920-5861\(01\)00473-4](https://doi.org/10.1016/S0920-5861(01)00473-4).
- [6] H.A. Atwater, A. Polman, *Nat. Mater.* 9 (2010) 205–213, <https://doi.org/10.1038/nmat2629>.
- [7] D.J. Dingley, M. Longden, J. Weinbren, J. Alderman, *Scanning Microsc.* 1 (1987) 451–456.
- [8] N.C.K. Lassen, D.J. Jensen, K. Conradsen, *Scanning Microsc.* 6 (1992) 115–121.
- [9] X. Huang, Q. Liu, *Ultramicroscopy* 74 (1998) 123–130, [https://doi.org/10.1016/S0304-3991\(98\)00033-3](https://doi.org/10.1016/S0304-3991(98)00033-3).
- [10] S. Zaefferer, *J. Appl. Crystallogr.* 33 (2000) 10–25, <https://doi.org/10.1107/S0021889899010894>.
- [11] E.F. Rauch, L. Dupuy, *Arch. Metall. Mater.* 50 (2005) 87–99.
- [12] D.J. Dingley, *Microchim. Acta* 155 (2006) 19–29, <https://doi.org/10.1007/s00604-006-0502-4>.
- [13] G. Wu, S. Zaefferer, *Ultramicroscopy* 109 (2009) 1317–1325, <https://doi.org/10.1016/j.ultramic.2009.06.002>.
- [14] J. Gjønnes, V. Hansen, A. Kverneland, *Microsc. Microanal.* 10 (2004) 16–20, <https://doi.org/10.1017/S1431927604040279>.
- [15] E.F. Rauch, J. Portillo, S. Nicolopoulos, D. Bultreys, S. Rouvimov, P. Moelck, Z. Kristallogr. 225 (2010) 103–109, <https://doi.org/10.1524/zkri.2010.1205>.
- [16] H.H. Liu, S. Schmidt, H.F. Poulsen, A. Godfrey, Z.Q. Liu, J.A. Sharon, X. Huang, *Science* 332 (2011) 833–834, <https://doi.org/10.1126/science.1202202>.
- [17] K. Lu, J. Lu, J. Mater. Sci. Technol. 15 (1999) 193–197, <https://doi.org/10.1007/s11837-999-0047-1>.
- [18] W.P. Tong, N.R. Tao, Z.B. Wang, J. Lu, K. Lu, *Science* 299 (2003) 686–688, <https://doi.org/10.1126/science.1080216>.
- [19] X. Zhang, N. Hansen, Y. Gao, X. Huang, *Acta Mater.* 60 (2012) 5933–5943, <https://doi.org/10.1016/j.actamat.2012.07.037>.
- [20] G. Liu, J. Lu, K. Lu, *Mat. Sci. Eng. A-Struct.* 286 (2000) 91–95, [https://doi.org/10.1016/S0921-5093\(00\)00686-9](https://doi.org/10.1016/S0921-5093(00)00686-9).
- [21] X. Wang, Y.S. Li, Q. Zhang, Y.H. Zhao, Y.T. Zhu, *J. Mater. Sci. Technol.* 33 (2017) 758–761, <https://doi.org/10.1016/j.jmst.2016.11.006>.
- [22] T.H. Fang, W.L. Li, N.R. Tao, K. Lu, *Science* 331 (2011) 1587–1590, <https://doi.org/10.1126/science.1200177>.
- [23] D.A. Hughes, N. Hansen, *Phys. Rev. Lett.* 87 (2001), <https://doi.org/10.1103/PhysRevLett.87.135503>, 135503.
- [24] C. Hong, X. Huang, N. Hansen, *IOP Conf. Ser.: Mater. Sci. Eng.* 89 (2015) 012026, <https://doi.org/10.1088/1757-899X/89/1/012026>.
- [25] S.Q. Deng, A. Godfrey, W. Liu, N. Hansen, *Scripta Mater.* 117 (2016) 41–45, <https://doi.org/10.1016/j.scriptamat.2016.02.007>.
- [26] Q.Y. He, M. Zhu, Q.S. Mei, C.S. Hong, G.L. Wu, X. Huang, *IOP Conf. Ser.: Mater. Sci. Eng.* 219 (2017) 012025, <https://doi.org/10.1088/1757-899X/219/1/012025>.
- [27] X. Huang, M. Zhu, Z.Q. Feng, Q.Y. He, C.S. Hong, G.L. Wu, S. Schmidt, Grain Orientation Mapping in Gradient Nanostructured Metals Produced by Surface Plastic Deformation, 38th Risø International Symposium on Materials Science, Technical University of Denmark, 2017, pp. 55–62. https://orbit.dtu.dk/files/152363251/Risoe_Symposium_2017_Huang.pdf.
- [28] F.J. Humphreys, *J. Mater. Sci.* 36 (2001) 3833–3854, <https://doi.org/10.1023/a:1017973432592>.
- [29] D.R. Steinmetz, S. Zaefferer, *Mater. Sci. Technol.* 26 (2013) 640–645, <https://doi.org/10.1179/026708309x12506933873828>.
- [30] R.R. Keller, R.H. Geiss, *J. Microsc.* 245 (2012) 245–251, <https://doi.org/10.1111/j.1365-2818.2011.03566.x>.
- [31] P.W. Trimby, *Ultramicroscopy* 120 (2012) 16–24, <https://doi.org/10.1016/j.ultramic.2012.06.004>.
- [32] www.nanomegas.com.
- [33] Z.Q. Feng, Y.X. Chen, G.L. Wu, Y.Q. Yang, *IOP Conf. Ser. Mater. Sci. Eng.* 89 (2015) 12023, <https://doi.org/10.1088/1757-899X/89/1/012023>, 012023.
- [34] Y. Chen, Y. Yang, Z. Feng, B. Huang, X. Luo, G. Zhao, *Philos. Mag. A* 97 (2016) 28–42, <https://doi.org/10.1080/14786435.2016.1243266>.
- [35] Y. Chen, Y. Yang, Z. Feng, G. Zhao, B. Huang, X. Luo, Y. Zhang, W. Zhang, *Mater. Char.* 123 (2017) 189–197, <https://doi.org/10.1016/j.matchar.2016.11.021>.
- [36] A. Kobler, C. Kübel, *Ultramicroscopy* 173 (2017) 84–94, <https://doi.org/10.1016/j.ultramic.2016.07.007>.
- [37] M. Liu, Y. Pang, B. Zhang, P. De Luna, O. Voznyy, J. Xu, X. Zheng, C.T. Dinh, F. Fan, C. Cao, F.P. de Arquer, T.S. Safaei, A. Mephram, A. Klinkova, E. Kumacheva, T. Filleter, D. Sinton, S.O. Kelley, E.H. Sargent, *Nature* 537 (2016) 382–386, <https://doi.org/10.1038/nature19060>.
- [38] B. Wu, N. Zheng, *Nano Today* 8 (2013) 168–197, <https://doi.org/10.1016/j.nantod.2013.02.006>.
- [39] X. Wang, M. Vara, M. Luo, H. Huang, A. Ruditskiy, J. Park, S. Bao, J. Liu, J. Howe, M. Chi, Z. Xie, Y. Xia, *J. Am. Chem. Soc.* 137 (2015) 15036–15042, <https://doi.org/10.1021/jacs.5b10059>.
- [40] X. Huang, M. Zhu, Z.Q. Feng, Q.Y. He, G.L. Wu, S. Schmidt, in: S. Dhar, S. Faester, A. Godfrey, N. Hansen, C. Hong, X. Huang, D. Juul Jensen, O.V. Mishin, T. Yu, Y. Zhang (Eds.), *Proceedings of in: “Microstructural Design”, the 38th Risø National*

- Symposium on Materials Science, Technical University of Denmark, Roskilde, 2017, pp. 55–62.
- [41] W.Q. Zhu, G.L. Wu, T.L. Huang, S. Schmidt, L. Zhang, Z.Q. Feng, J.N. Deng, X. Huang, Submitted to Thermec (2020).
- [42] M. Guizar-Sicairos, S.T. Thurman, J.R. Fienup, Opt. Lett. 33 (2008) 156–158, <https://doi.org/10.1364/ol.33.000156>.
- [43] P.A. Midgley, M. Weyland, Ultramicroscopy 96 (2003) 413–431, [https://doi.org/10.1016/s0304-3991\(03\)00105-0](https://doi.org/10.1016/s0304-3991(03)00105-0).
- [44] R.E.W. Rafael C. Gonzalez, Steven L. Eddins, Digital Image Processing Using MATLAB, Gatesmark Publishing 2009.
- [45] <https://www.mathworks.cn/help/images/ref/imadjust.html?requestedDomain=cn>.
- [46] N. Otsu, IEEE T. Syst. Man Cyb. 9 (1979) 62–66, <https://doi.org/10.1109/tsmc.1979.4310076>.
- [47] D. Bradley, G. Roth, J. Graph. Tool. 12 (2011) 13–21, <https://doi.org/10.1080/2151237x.2007.10129236>.
- [48] G. Wu, D. Juul Jensen, Mater. Char. 59 (2008) 794–800, <https://doi.org/10.1016/j.matchar.2007.06.015>.
- [49] C. Zhang, A. Suzuki, T. Ishimaru, M. Enomoto, Metall. Trans. A 35A (2004), <https://doi.org/10.1007/s11661-004-0141-5>, 1927–32.
- [50] M. Groeber, S. Ghosh, M.D. Uchic, D.M. Dimiduk, Acta Mater. 56 (2008) 1257–1273, <https://doi.org/10.1016/j.actamat.2007.11.041>.
- [51] A.S. Eggeman, R. Krakow, P.A. Midgley, Nat. Commun. 6 (2015) 7, <https://doi.org/10.1038/ncomms8267>.
- [52] J.M. Thomas, R.K. Leary, A.S. Eggeman, P.A. Midgley, Chem. Phys. Lett. 631–632 (2015) 103–113, <https://doi.org/10.1016/j.cplett.2015.04.048>.
- [53] W. Sinkler, L.D. Marks, Z. Kristallogr. 225 (2010) 47–55, <https://doi.org/10.1524/zkri.2010.1199>.
- [54] N. Kawase, M. Kato, H. Nishioka, H. Jinnai, Ultramicroscopy 107 (2007) 8–15, <https://doi.org/10.1016/j.ultramic.2006.04.007>.
- [55] A.M. Nie, Y.Q. Bu, J.Q. Huang, Y.C. Shao, Y.Z. Zhang, W.T. Hu, J.B. Liu, Y.B. Wang, B. Xu, Z.Y. Liu, H.T. Wang, W. Yang, Y.J. Tian, J. Mat. (2020), <https://doi.org/10.1016/j.matt.2020.02.011>.
- [56] Y.Z. Zhang, Y.Q. Bu, X.Y. Fang, H.T. Wang, Sci. China Technol. Sci. (2020). <https://arxiv.org/abs/2001.07074>. in press.